Fast volumetric imaging with line-scan confocal microscopy by electrically tunable lens at resonant frequency

KHUONG DUY MAC,[1] [iD] **MUHAMMAD MOHSIN QURESHI,[2] MYEONGSU NA,[3] SUNGHOE CHANG,[3,4] TAE JOONG EOM,[5,6] HYUNSOO SHAWN JE,[7,8] YOUNG RO KIM,[9,10] HYUK-SANG KWON,[1,13] AND EUIHEON CHUNG[1,11,12,14]**

[1]*Department of Biomedical Science and Engineering, Gwangju Institute of Science and Technology, Gwangju 61005, Republic of Korea*
[2]*Division of Biophysics and Bioimaging, Princess Margaret Cancer Centre, Toronto, ON, Canada*
[3]*Department of Physiology and Biomedical Sciences, Seoul National University College of Medicine, 103 Daehak-ro, Jongno-gu, 03080 Seoul, Republic of Korea*
[4]*Neuroscience Research Institute, Seoul National University College of Medicine, 103 Daehak-ro, Jongno-gu, 03080 Seoul, Republic of Korea*
[5]*Department of Cogno-Mechatronics Engineering, Pusan National University, Busan, 46241, Republic of Korea*
[6]*Engineering Research Center (ERC) for Color-modulated Extra-sensory Perception Technology, Pusan National University, Busan, 46241, Republic of Korea*
[7]*Signature Program in Neuroscience and Behavioural Disorders, Duke-National University of Singapore (NUS) Medical School, 8 College Road 169857, Singapore*
[8]*Advanced Bioimaging Center, Academia, Ngee Ann Kongsi Discovery Tower Level 10, 20 College Road, 169855, Singapore*
[9]*Athinoula A. Martinos Center for Biomedical Imaging, Massachusetts General Hospital, Charlestown, Massachusetts 02129, USA*
[10]*Department of Radiology, Harvard Medical School, Boston, Massachusetts 02115, USA*
[11]*AI Graduate School, Gwangju Institute of Science and Technology, Gwangju 61005, Republic of Korea*
[12]*Research Center for Photon Science Technology, Gwangju Institute of Science and Technology, Gwangju 61005, Republic of Korea*
[13]*hyuksang@gist.ac.kr*
[14]*ogong50@gist.ac.kr*

Abstract: In microscopic imaging of biological tissues, particularly real-time visualization of neuronal activities, rapid acquisition of volumetric images poses a prominent challenge. Typically, two-dimensional (2D) microscopy can be devised into an imaging system with 3D capability using any varifocal lens. Despite the conceptual simplicity, such an upgrade yet requires additional, complicated device components and usually suffers from a reduced acquisition rate, which is critical to properly document rapid neurophysiological dynamics. In this study, we implemented an electrically tunable lens (ETL) in the line-scan confocal microscopy (LSCM), enabling the volumetric acquisition at the rate of 20 frames per second with a maximum volume of interest of $315 \times 315 \times 80$ μm^3. The axial extent of point-spread-function (PSF) was 17.6 ± 1.6 μm and 90.4 ± 2.1 μm with the ETL operating in either stationary or resonant mode, respectively, revealing significant depth axial penetration by the resonant mode ETL microscopy. We further demonstrated the utilities of the ETL system by volume imaging of both cleared mouse brain *ex vivo* samples and *in vivo* brains. The current study showed a successful application of resonant ETL for constructing a high-performance 3D axially scanning LSCM (asLSCM) system. Such advances in rapid volumetric imaging would significantly enhance our understanding of various dynamic biological processes.

1. Introduction

For the mechanistic dissection of operational principles of biological phenomena, visualization of dynamic cellular activities *in vivo* is of great importance [1]. Compared to other acquisition methods of spatiotemporal traits, real-time recording of the biological structure and function has only been feasible by the optical approaches with high fidelity [2–4]. Among the technical features of modern optical imaging, rapid 3D volumetric visualization is a highly focused area of research for achieving precise documentation of biophysical cascades. For this purpose, among the currently available modalities, two-photon microscopy was implemented with axial scanning electrically tunable lens (ETL) to yield 3D recordings of single-cell and calcium-activation images [5]. However, widespread use of the two-photon ETL system can be restricted due to the limited acquisition rate in volumetric imaging and practical difficulties in the optimization of two-photon imaging conditions. On the other hand, precluding such limitations, confocal laser scanning microscopy offers several important benefits, such as optical sectioning for 3D imaging and high-resolution capability, enabling the efficient 3D visualization of dynamic biological processes [6–8].

In the recent past, several innovative advances in confocal microscopy have been developed to augment 3D imaging capabilities. In addition to the traditional 3D method, which is typically achieved by moving the sample in z-direction [9], multiple confocal strategies have been proposed to enhance the image acquisition speed: 1) rapid axial scanning of multiple focal planes using an electrically tunable lens (ETL) [10,11], 2) utilizing mechanical devices such as deformable mirrors [12], spatial light modulator [13], and adaptive lens [14]. Although such improvements could achieve 3D imaging at a relatively high resolution, the axial scanning rate ultimately limits the volumetric acquisition rate. Alternative strategies employing multiple pinholes/slits/prisms [15–17] enabled volumetric imaging at a video rate for a relatively large field of view. However, these methodologies intrinsically suffer from the limited number of layers in the axial direction as well as the relatively low optical resolution.

Here, in response to such shortcomings, we developed a microscopy technique that enables the acquisition of the projected high-resolution 3D images of an entire volume at a video rate, removing the constraint on the number of axial layers. Specifically, by combining the working principle of the resonant ETL, axially scanned line-scan confocal microscopy (asLSCM) was conceptually devised and constructed for 3D *in vivo* imaging. Traditionally, the line-scan confocal microscopy is performed by the addition of a cylindrical lens, providing a confocal point on a single axial focus at the speed of approximately a hundred 2D frames per second. To take advantage of such a high scan speed, ETL was conjugated to the line-scan confocal microscopy for axially averaging each line scan point signal in the current experimental setup. Conventional confocal microscopy with an ETL had a limited acquisition speed due to its 3-axis scanning scheme: two in the lateral and one in the axial direction. In contrast, our asLSCM has only one lateral scanning with rapid-axial averaging, which can boost the rate of volumetric imaging. In this report, we demonstrated the utilities of the newly-designed asLSCM by *ex vivo* imaging of fluorescently labeled neurons and *in vivo* imaging of cerebral blood vessels.

2. Methods

2.1. Optical implementation

The schematic diagram of the ASLSCM is shown in Fig. 1(a). Briefly, in the illumination path, a 475nm laser (Changchun New Industries Optoelectronics Technology Co., Ltd., China, MBL-III-473-100mW) was used as an excitation source. The laser beam size was magnified by three times using a 4-f system (f = 50 mm and f = 150 mm) before it propagated into a cylindrical lens (f_{cyl} = 50 mm), which generated a line pattern parallel to the x-axis at the image plane (side view). The cylindrical lens was shown in the front view as well as a side view (Fig. 1(a)). A

one-axis scanning mirror (Thorlabs, GVS002) was located right after the cylindrical lens to perform as the sweeping light source at a range of 2-degree angles. This laser swept parallel to the y-axis (front view) as shown in Fig. 1(b) to combine the line pattern from the cylindrical lens for 2D scanning. The elliptical beam propagated to the scan lens (f_{scan} = 60 mm) and an achromatic doublet lens (f_{L1} = 100 mm) (Fig.1a). Given that the objective lens was predetermined with the specific numerical aperture value, which was directly correlated with the resolution and the field of view [18], the beam-sheet was connected with the other 4-f system to balance these limitations. This 4-f system consisted of the ETL (Optotune, EL-10-30-C-VIS-LD, generated at 140mA) and the tube lens (f_{TL} = 150 mm) to fill the light at the back focal plane of the objective lens (Olympus, 20X 0.5 NA, water immersion, UMPLFLN20XW. A dichroic mirror (Semrock, FF552-Di02-25 × 36) was placed between the first tube lens and the 4-f system of the ETL, to perform fast axial scanning, and to guide the detection path followed by the scan path (Fig. 1(b)). The resonant frequency of the axial scanning using the ETL (~400 Hz) was 20 times faster than the speed of the lateral image scanning (~20 Hz). Therefore, the axially averaged lines were sufficient for generating a projected 3D image with the axial penetration of the point-spread function (PSF) in the line scan mode. The current system was modified from the original configuration to overcome the problem of unstable lateral resolution due to the ETL focal length change (Supplement 1, Figure S1).
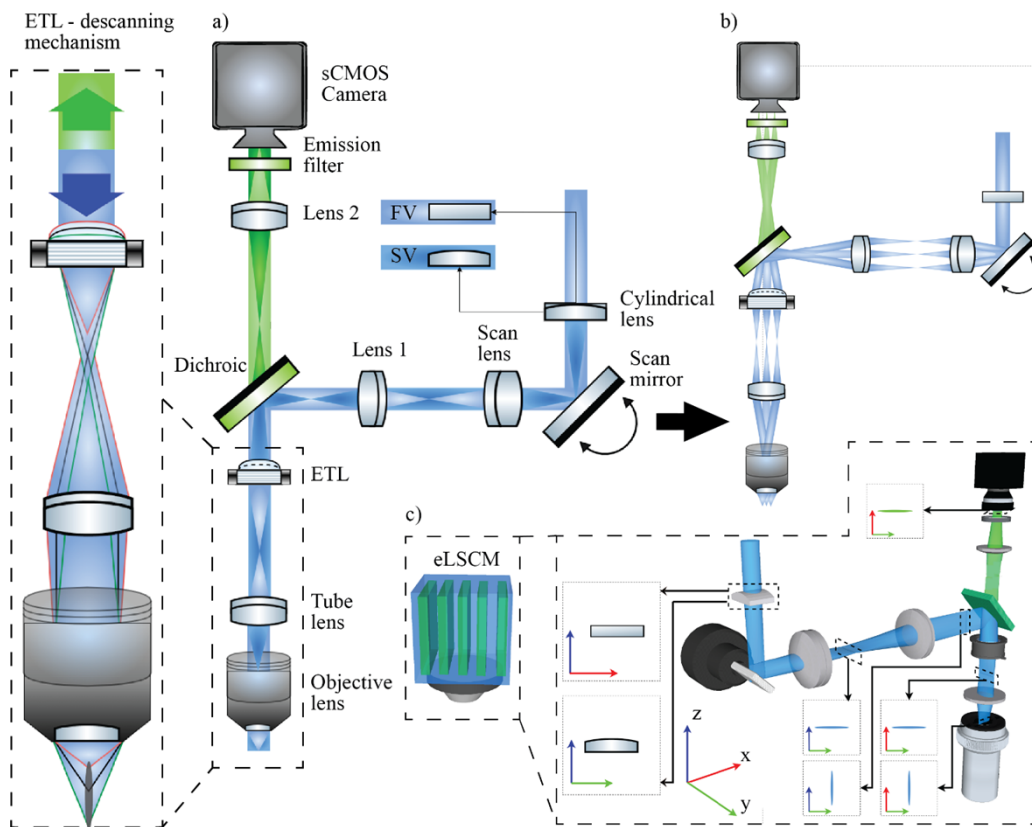

Fig. 1. The schematic diagram for ETL-based asLSCM where a) the working principle of the ETL-based ASLSCM in front view and side view based on the cylindrical lens, b) the scanning view and direction of the scan mirror on the system, c) the 3D view of the system. FV: front view, SV: side view.

In the detection path, the emitted fluorescent signal propagates back to the tube lens and the ETL, enabling an "ETL descanning mechanism". A plano-convex lens (f_{L2} = 60mm) was placed between the dichroic mirror and a detector to generate a line pattern at the detector surface. In our system, an sCMOS camera (PCO.edge 4.2 mono, PCO imaging) was used in a rolling shutter mode to capture the full image of 360×360 pixels at 20 fps. The camera exposure time was synchronized to the scanner signal, which resulted in the effective formation of a virtual confocal slit. All the camera components and devices were driven by open-source software (µ-Manager 1.4) [19]. The beam profiles at different locations were illustrated in XYZ coordinates as depicted in the Fig. 1(c).

2.2. *PSF measurement with fluorescent beads*

Spatial resolution was measured using fluorescent beads (0.5 µm, Thermo Scientific, G500) [20]. The sample holder (Thorlabs, MAX3SLH) was mounted on a translation stage (Sutter Instrument, MPC-200). The ETL is generated in stationary mode and acquired the image of the bead at continuous layers with the step size is $\Delta z = 0.5$ µm. The full volume images of the bead are then reconstructed by the 3D viewer function in ImageJ for images in the z-direction [21]. We measured the intensity cross-section profile of each fluorescent bead image in either XY or XZ direction. The intensity data from each bead image was normalized to calculate the full width at half maximum. The image at a single layer was taken three times then did the average to give the most accurate axial PSF profile.

2.3. *Ex vivo imaging of neurons in a cleared brain slice*

A coronal section of a cleared brain was prepared from a Thy1-eYFP mouse [22]. The experiment was performed in two different modes. First, the translation stage moved the sample toward the objective lens with a step size of $\Delta z = 1.0$ µm to acquire full volumetric imaging with the stationary ETL. Second, the image of the cleared brain in the same region was acquired in the resonant ETL mode without moving the translation stage. To visualize the volumetric stack in a 2D image, we used the Time-Lapse Color-Coded Plugins of ImageJ software.

2.4. *In vivo imaging of blood vessels in a mouse with a cranial window*

An open skull craniotomy with a diameter of 5 mm was prepared using C57BL/6 mice. We placed a circular cover glass with a diameter of 6 mm on the open skull and sealed it with dental cement. We used Zoletil/Xylazine mixed in saline solution for anesthesia with the dose of 60/10 mg/kg body weight. The body temperature of an animal was kept stable at 37.0–37.5°C. For *in vivo* blood vessels, imaging was also performed in two different imaging modes. First, after identifying the target blood vessels, the volumetric blood vessel images were taken with the step size of $\Delta z = 1.00$ µm with a stationary ETL mode. Next, the same area was imaged using a resonant ETL mode for 7.5 seconds at 20 volumes per second. During the post-processing, we used the Time-Lapse Color-Coded Plugins of ImageJ software to highlight the relative depth of blood vessels.

3. Result

3.1. *ETL characterization with the driving frequency*

An ETL can change the focal length based on the driving current [23]. When the applied current is shifted, the ETL requires a certain settling time for its stabilization, which limits the ETL's maximum rate of synchronization during imaging [24]. As each ETL has its unique settling time and damping property [24], we validated the effect of the driving current frequency on the

scanning range of our system in Fig. 2, where the settling frequency was defined as:

$$f_{st} = \frac{1}{settling\ time} \tag{1}$$

Theoretically, if the driving frequency of the ETL is lower than the settling frequency, the scanning range will be dependent on the applied current frequency. However, the current ETL f_{st} was 60 Hz, which was too slow to combine with the lateral scanning for video-rate asLSCM imaging for a wide area. If the modulation frequency is higher than the settling frequency of the ETL but is lower than the resonant frequency, as in Fig. 2(a), the ETL will be over-damped and cannot achieve the desired axial penetration of a focal length. Therefore, the scanning range will be determined by the ETL driving frequency. At resonant frequency, the activation of ETL is synchronized with the damping properties, which results in maximizing the scanning range of the ETL (Fig. 2(b)). In contrast, when the ETL is driven at a frequency higher than the resonance frequency, it is over-damped, resulting in a reduced scanning range (Fig. 2(c)).
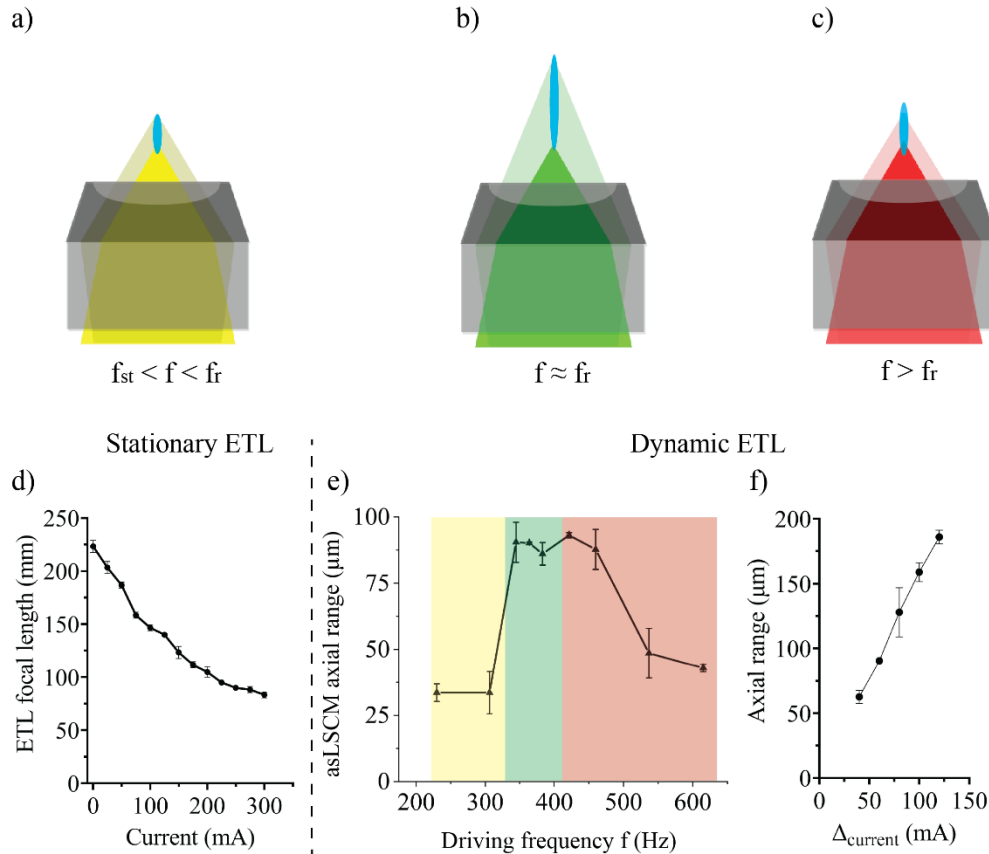

Fig. 2. The effect of driving frequency on the axial ETL scanning range. When the driving frequency of ETL is a) greater than settling frequency but lower than the resonant frequency, b) approximately the resonant frequency, c) greater than the resonant frequency, the axial penetration of the point-spread function varies (noted in blue). d) the stationary ETL focal length decreases with increasing applied current, e) the dynamic ETL focal scanning range depends on the driving frequency of ETL when the driving current was I(t), and f) the scanning range of the system (in micrometer) in different scanning range (in current) of the ETL.

We first calibrated the ETL focal length with respect to the driving current. When the frequency was set at 0 Hz (stationary ETL), the focal position was identified and recorded at each driving current. For example, the focal length was ∼ 130 mm with a current of 140 mA. When the current was increased from 0 to 300 mA, the focal length decreased from 230 to 90 mm as shown in Fig. 2(d). The focal scanning range varied depending on the driving frequency when the frequency was non-zero (dynamic ETL). For understanding the ETL characteristics, we set the current in the range between 110 mA and 170 mA, which corresponds to the focal length of approximately 120 mm to 150 mm, respectively. This configuration ensures to fill the back aperture of the objective lens via the tube lens with focal length of 150 mm before entering into the objective lens (Fig. 1 left box).

The ETL driving current at resonance can be described as:

$$I(t) = I_0 sin(2\pi ft) + I_{st}, (I_0 = 30\ mA, I_{st} = 140\ mA) \tag{2}$$

where f_{st}: settling frequency, f: driving frequency of ETL, f_r: resonant frequency, I_0: dynamic current amplitude in ETL, I_{st}: current at the stable stage of ETL. The axial scanning range with respect to the ETL driving frequency is shown in Fig. 2(e). The maximum scanning range was obtained with the driving frequency range of 340 ∼ 420 Hz, and we chose 400 Hz (as the resonant frequency) for our ETL-based asLSCM.

To determine the optimal penetration value of the axial PSF for imaging experiments, we characterized the relationship between the axial range and Δcurrent at the resonant frequency of 400 Hz (Fig. 2(f)). The measured axial scanning range of PSF of the system was proportional to Δcurrent. However, higher axial scanning ranges accompanied significant FOV changes, thus we chose Δcurrent of 60 mA for the 90 μm axial range in our study (with only ±5% FOV change, Supplement 1, Figure S4).

3.2. 3D asLSCM point-spread function (PSF) measurement

To measure the PSF, we employed two ETL modes to compare resolutions by different modes, i.e., stationary and resonant ETL modes. With the stationary ETL mode at a driving current of 140 mA, the lateral full-width-half-maximum (FWHM) was evaluated as $\delta x = 2.0 \pm 0.5$ μm and $\delta y = 1.8 \pm 0.1$ μm (n = 3), indicating a slightly better resolution in the confocal axis (y-direction) while the axial resolution FWHM was $\delta z = 17.6 \pm 1.6$ μm (n = 3) (Fig. 3(a)). With the resonant ETL mode at 400 Hz, a sinusoidal current from 110 mA to 170 mA was used with the corresponding ETL focal lengths of 120 mm to 150 mm, respectively. The lateral FWHM was found as $\delta x = 3.2 \pm 0.3$ μm and $\delta y = 2.9 \pm 0.4$ μm (n = 3). The axial FWHM was elongated by 5.1 times to $\delta z = 90.4 \pm 2.1$ μm (n = 3) (Fig. 3(b)). We acknowledged that the sinusoidal nature of the driving current of an ETL might result in higher intensity values at two peaks due to transient slowdown. While brighter at the top position, this phenomenon might be beneficial for imaging a scattering medium due to the elevated signals at deeper layers. On the other hand, the lateral resolution remained approximately equivalent within a one-micron range between the two modes (Supplement 1, Fig. S2). Further experiments on ETL-associated aberrations are described in Supplement 1, Fig. S3.

The FWHM data at different depths are shown in Fig. 3(c) and Fig. 3(e), where each color represents the corresponding plane in the axial direction. We observed that the most significant change in normalized intensity in the axial direction was approximately 11.1%, indicating that the axial penetration of PSF's lateral resolution remained consistent throughout different depths.

To evaluate the distortion generated by the ETL, we further measured the Strehl ratio of each lateral image at different axial positions of PSF as shown in Fig. 3(e). The Strehl ratios of the system measured compare to the center point at the layer 40 μm, 15 μm, -10 μm and -30 μm were 0.80 ± 0.11, 0.85 ± 0.03, 0.91 ± 0.05 and 0.77 ± 0.08 (n = 3), respectively. The Strehl ratios confirm that there were only small distortions in the axial direction when the ETL was activated.
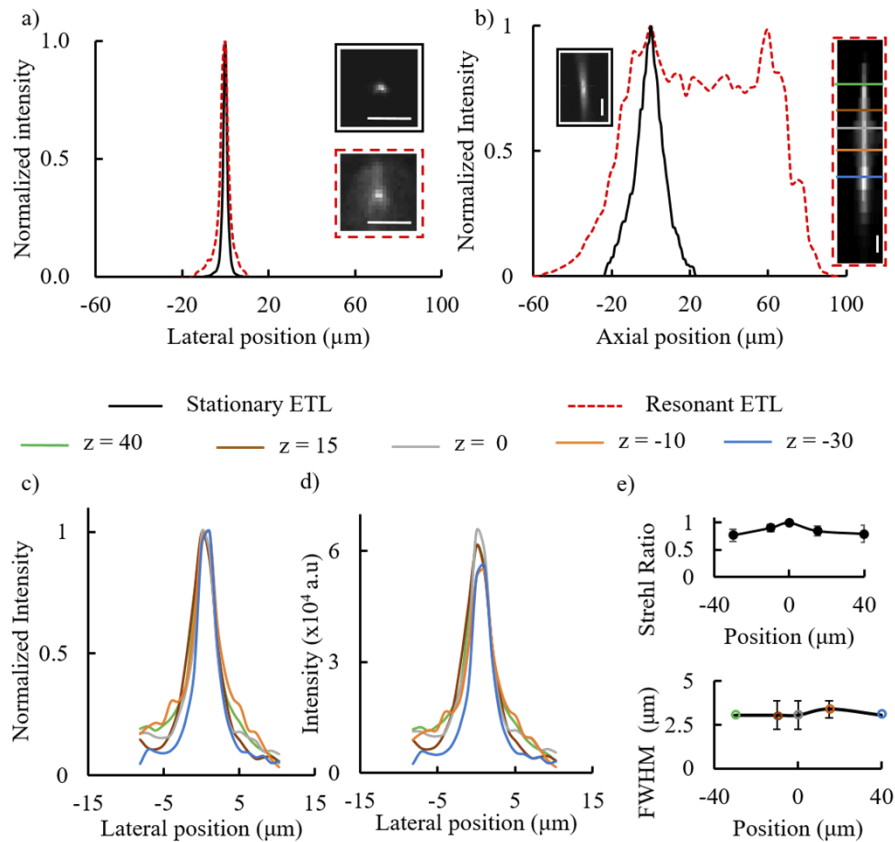
Fig. 3. **PSF measurement in XY and XZ transverse direction using 0.5 μm fluorescent beads,** a) the lateral FWHM value, b) the axial FWHM value of the system when ETL is in the stationary mode at 140 mA and in the resonant mode from 110 mA to 170 mA at ~400 Hz, where the profile of lateral PSF were chosen from the five layers in the axial direction at the resonant ETL mode, c) normalized intensity, d) full intensity profile, e) the Strehl ratio of the four layers compare to layer at zero position and the FWHM value in lateral direction of each layer (n = 3). Scale bar: 10 μm

The extended penetration of PSF was systematically effective as the calculated Strehl ratios were relatively high at ~0.8, along with the fact that there were no considerable differences among the FWHM values from the different lateral layers.

3.3. Volumetric imaging of cleared brain ex vivo

After the PSF characterization, we imaged cleared brain sections harvested from a Thy1-eYFP transgenic mouse (Fig. 4(a)). Cortical regions of the brain were imaged using our ETL-based ASLSCM system. The experiment was performed in two different modes: stationary and resonant ETL modes with the relevant driving currents, I(t). In the stationary ETL mode, we imaged neurons at each layer with the step size of $\Delta z = 1$ μm for a total range of 80 μm. Figure 4(b) shows the layer imaging results at the middle plane of the brain (z = 40 μm). Next, multi-layer z-stack images are shown in Fig. 4(c), where the color illustrates the axial positions of the layer (Fig. 4(d))., Identical cortical neurons were selected for imaging in the resonant ETL mode (Fig. 4(e)) at z = 0 μm, which was acquired with 20 fps and averaged for 5 seconds covering a volume of $315 \times 315 \times 80$ μm³. (see Visualization 1).
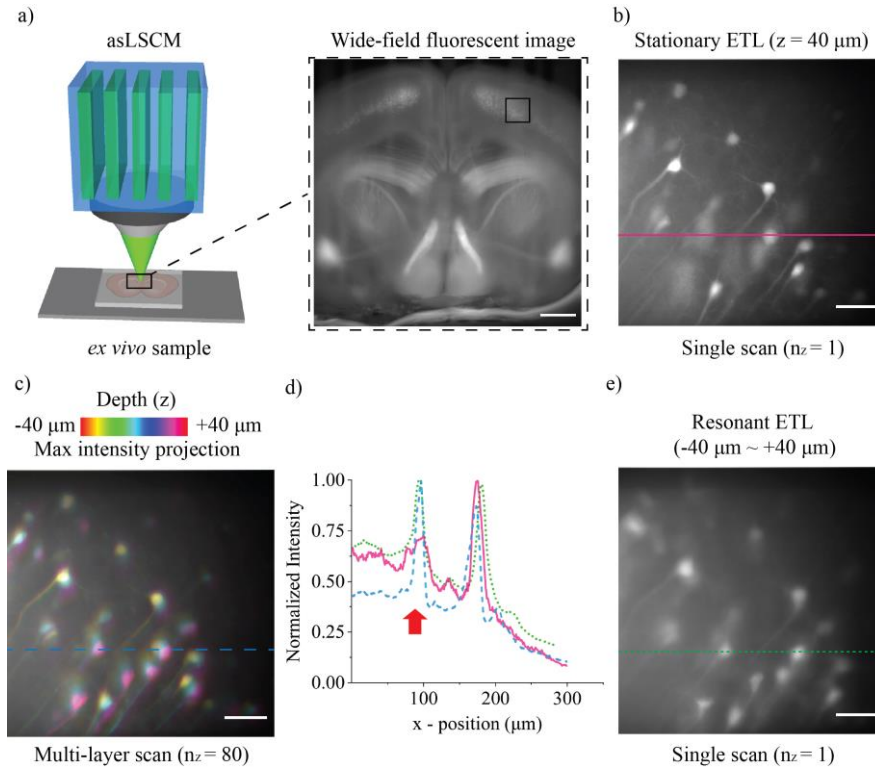
Fig. 4. *Ex vivo* **volumetric imaging of cleared brain slice from Thy1-eYFP mouse**. a) wide-field fluorescence image, scale bar: 500 μm, (b, c) cortical neurons imaged in the stationary ETL mode with the step size of Δz = 1 μm for the total of ~80 layers; the layer image at 40 μm and maximum intensity projection (MIP) image, respectively e) cortical neurons imaged in the resonant ETL mode with an extended depth of field of asLSCM, d) the normalized intensity plot showing profiles through the cross-sectional line from the stationary, MIP, and resonant images; b), c) and e), respectively (see Visualization 1). Scale bar: 50 μm.

To demonstrate the axial penetration of PSFs, we performed a single scan using ETL in the resonant mode, as shown in Fig. 4(e). The intensity profiles of the neuronal signals located along the identical line are shown in three modes: the single scan in the resonant ETL mode, single and multi-layer scan in the stationary ETL mode in Fig. 4(d). While the normalized intensities of single scan in the resonant mode and multi-layer scan in the stationary mode were closely matched, the data plotted from the single layer scan in the stationary mode indicated a discrepancy (red arrow), revealing the loss of signal from a neuron axially located in the out-of-focus area within the brain cortex. The findings demonstrate the single frame imaging capability of ETL-based asLSCM instantaneously amassing the averaged signal from 80 μm-thick slabs in the sample. However, due to the ETL-associated aberration that could change focal lengths, background noise in the resonant ETL mode imaging (Fig. 4(e)) was higher than that from the multi-layer scan imaging in the stationary ETL mode (Fig. 4(c)).
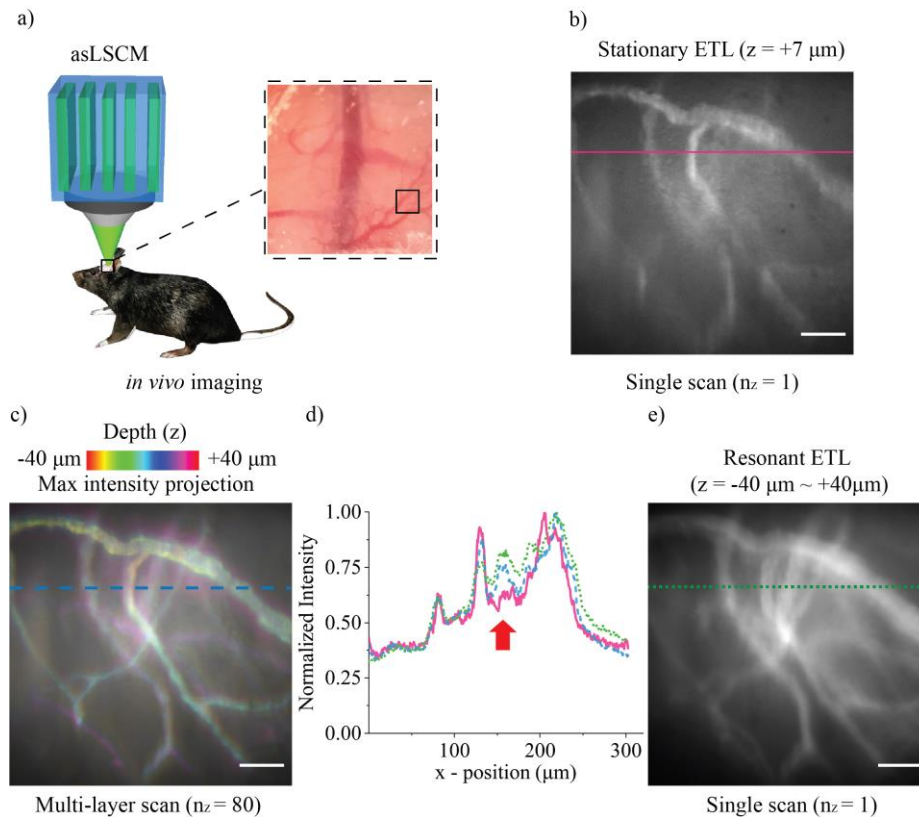
Fig. 5. Imaging blood vessels in the mouse brain *in vivo*. a) Schematic diagram of *in vivo* brain imaging experiment, b) the blood vessels imaging of +7 μm-layer in the stationary ETL mode, c) total ~80 layers (with the step size $\Delta z = 1$ μm) combined; the volumetric image color-coded by depth of the blood vessels, e) the single extended depth of field scan for video-rate imaging of blood vessels in the resonant ETL mode for 7.5 seconds, and d) the normalized intensity plot showing profiles from the images (pink line: cross-section of the single scan in the stationary mode, blue line: cross-section of stacked multilayer image in the stationary mode, green line: cross-section of the extended depth of field volumetric image in the resonant mode)(see Visualization 2). Scale bar: 50 μm.

3.4. In vivo volumetric imaging of blood vessels of mouse brain

For *in vivo* experiments, we performed a craniotomy to place an optical window [25]. Under anesthesia, the animal was injected with fluorescein isothiocyanate – Dextran 500 kDa-Conjugate (FITC) via retro-orbital injection [26,27].

FITC-labeled cerebral vessels were visualized with the asLSCM, as shown in Fig. 5(a). The asLSCM was operated in both stationary and resonant ETL modes, alternatively. In the stationary mode, we imaged blood vessels in multiple 2D planes using a translation stage; each plane produced one image at 20 fps with an FOV of 315×315 μm^2. Next, we captured the image of one selected layer (Fig. 5(b)) before 3D imaging with an axial range of 80 μm (Fig. 5(c)). In the resonant ETL mode, we imaged blood vessels with the same FOV (Fig. 5(e)); the full videos of a 3D stacked image and the ETL-based ASLSCM of cerebral blood vessels are shown in Visualization 2.

Line intensity profiles were taken from the same location as the images obtained from 3 different imaging modes. In the stationary mode, the cross-section intensity profiles were obtained from both the single-layer scan (red line) and the max intensity projection image from the multilayer scan (blue dotted line). In the resonant mode, the line intensity profile was taken from an image acquired and averaged over a total scan time of 7.5 seconds (green dotted line). All intensity profiles were normalized to highlight differences between images acquired from three different modes (Fig. 5(d)). The peak intensity levels grossly matched when we compared the results from the volumetric multi-layer scan in the stationary mode to the single scan result in the resonant ETL mode. However, upon comparing the single scans at video-rate between stationary and resonant modes, the loss of structural and functional information of blood vessels in stationary mode was evident in contrast to relatively more detailed visualization of blood vessels in the resonant mode (see red arrow in Fig. 5(d)). The current *in vivo* experimental data may contain movement-associated artifacts, which may arise from the intrinsic motion of blood vessels. We performed an additional experiment for structure visualization of the lens tissue paper stained with fluorescent FITC without any lateral movement artifact in the acquired images (see Visualization 3). Note the similarity of the structural images between the lens tissue paper and blood vessel geometry.

4. Discussion

We developed an extended depth-of-field, axially scanned line-scan confocal microscopy (asLSCM) by implementing the resonant ETL module to increase the PSF penetration in the axial direction achieving the imaging speed of 20 projected frames per second. In general, other techniques designed to axially expand the PSF by utilizing SLM or deformable mirror suffer from slow speed [12,13], layer-dependent magnification, and insufficient axial depth coverage [28]. Furthermore, the use of a phase mask also limits the field of view and axial detection range [29]. In the case of two-photon microscopy for fast volumetric imaging, the application of a line scan might be challenging due to the laser power limitation, for which the one fast axis scan with a tilted microlens array offered a viable option [30]. Although difficult in alignment, the use of the Bessel beam allows simultaneous generation of the elongated PSF in two-photon microscopy, which is not feasible for single-photon excitation due to significant side-lobes [31,32], suggesting further challenges in fast volumetric imaging. On the other hand, despite the possible aberration from the ETL limiting the spatial resolution, the proposed asLSCM scheme potentially enables real-time volumetric visualization of biological processes *in vivo*.

The axial range of asLSCM covers approximately 90.4 μm in depth which is 5.1 times elongated compared to stationary mode. The stationary mode lateral optical resolution of a traditional system with the ETL attached beneath the objective lens was 1.5 ± 0.1 μm, which was slightly better than 2.0 ± 0.5 μm that was obtained from the stationary mode imaging by ETL-based asLSCM (Fig. S2(b)). The lateral and axial resolution with and without ETL was characterized in Figure S2 in detail. The difference is probably because the current asLSCM was designed for volumetric imaging, not optimized for the stationary mode but set for imaging in the resonant mode. However, in the resonant ETL mode, the lateral optical resolution in our ETL-based asLSCM was roughly 3.2 ± 0.3 μm compared to 5.2 ± 0.1 μm from a conventional design setting (Fig. S2(c)). The degradation of lateral and axial optical resolutions under the stationary ETL mode is likely caused by the aberration of the ETL and additional blurring caused by the imperfect stability of the driving current, affecting the resultant PSF.

While the axial scanning range was roughly 80 μm in the current study, we could have increased it further as we did not drive the ETL to the maximum level. For our initial study, we used the $\Delta_{current}$ of 60 mA which corresponded to the axial scanning range of ~80 μm. The actual axial PSF could be expanded to nearly 200 μm by widening the scanning range of the ETL (Fig. 2(f)). In addition, the ETL-based asLSCM utilizes a system that is suitable for multiple types of the

objective lens, thus increasing the depth penetration of the PSF by choosing the objective lens properly [33,34]. Furthermore, the lateral scanning range and associated magnification are dependent on the position of the ETL and can be carefully characterized by optimizing the ETL position while maintaining the same image resolution [35]. Also, the resolution of the system might be further enhanced through the application of structure illumination technique [36]. The problem of non-uniform axial intensity distribution can be resolved by the synchronization of Pockels cell with the activation of ETL to compensate the excitation power dynamically."

By using an *ex vivo* brain slice, we demonstrated that our asLSCM system could acquire images at the maximum depth of $z = 80$ μm and volumetric dimensions of $315 \times 315 \times 80$ μm^3 at 20 fps. We also imaged *in vivo* cerebral blood vessels with the prospect of measuring blood flow velocity soon [37–39]. We expect that our asLSCM system can perform other *in vivo* experiments such as volumetric calcium imaging of sparsely labeled cortical neurons using fluorescent dyes or genetically encoded calcium indicators [16,17,40] to correlate neural activities during animal behaviors [41,42]. However, we acknowledge that the current approach can only be applied to sparsely labeled targets as the system provides an averaged axial projection image.

Previous microscopy techniques utilizing the axial penetration of PSF for volumetric imaging suffer from the compromised lateral and axial resolutions [16,43], or limited axial detection range [44]. Even the aberration caused by the phase mask along with the pinhole that is not compatible with slits may become problematic [32,45,46]. These aberrations could be reduced by adaptive optics [47,48] for further biological applications. The major caveat of our system is that the empirically determined resonant frequency and suboptimal use of the ETL module limit the speed of image acquisition and image quality, respectively. These shortcomings can be resolved by employing a TAG lens [49–51] or remote focusing [52,53]. In support of this notion, the resonance frequency of a commercially available TAG lens is 70 kHz (Mitutoyo), which can enhance the acquisition speed of our asLSCM to hundreds of frames per second. If we could precisely synchronize the scanner signal with the high-speed axial scanning unit, high-resolution imaging in the multi-plane construct might be achievable [54].

One important biomedical application of asLSCM could be quantitative blood flow measurement. The blood velocity can be estimated from the kymographic representation of volumetric projection images. However, due to the limited frame rate of the current asLSCM system (20 fps), current blood velocity measurement would be inadequate. With the enhanced volumetric imaging speed (e.g., use of TAG lens), the monitoring of dynamic blood flow could be feasible. Taken together, we developed a novel microscopy technique by combining the line-scan confocal microscopy and a resonant ETL-based axial scanning unit to axially lengthen the penetration of PSF, enabling volumetric projection imaging at video rate towards functional imaging of dynamic biological processes.

Supplemental document. See Supplement 1 for supporting content.

References

1. L. Shi, C. Zheng, Y. Shen, Z. Chen, E. S. Silveira, L. Zhang, M. Wei, C. Liu, C. de Sena-Tomas, K. Targoff, and W. Min, "Optical imaging of metabolic dynamics in animals," Nat Commun **9**(1), 2995 (2018).
2. W. Liu and J. Yao, "Photoacoustic microscopy: principles and biomedical applications," Biomed. Eng. Lett. **8**(2), 203–213 (2018).
3. P. K. Poola, M. I. Afzal, Y. Yoo, K. H. Kim, and E. Chung, "Light sheet microscopy for histopathology applications," Biomed. Eng. Lett. **9**(3), 279–291 (2019).
4. W. Mo, T. S. Chan, L. Chen, and N. Chen, "Quantitative characterization of optical and physiological parameters in normal breasts using time-resolved spectroscopy: in vivo results of 19 Singapore women," J. Biomed. Opt. **14**(6), 064004 (2009).
5. K. F. Tehrani, C. V. Latchoumane, W. M. Southern, E. G. Pendleton, A. Maslesa, L. Karumbaiah, J. A. Call, and L. J. Mortensen, "Five-dimensional two-photon volumetric microscopy of in-vivo dynamic activities using liquid lens remote focusing," Biomed. Opt. Express **10**(7), 3591–3604 (2019).
6. J. M. Jabbour, M. A. Saldua, J. N. Bixler, and K. C. Maitland, "Confocal endomicroscopy: instrumentation and medical applications," Ann Biomed Eng **40**(2), 378–397 (2012).
7. S. W. Paddock and K. W. Eliceiri, "Laser scanning confocal microscopy: history, applications, and related optical sectioning techniques," Methods Mol Biol **1075**, 9–47 (2014).
8. E. E. Freeman, A. Semeere, H. Osman, G. Peterson, M. Rajadhyaksha, S. Gonzalez, J. N. Martin, R. R. Anderson, G. J. Tearney, and D. Kang, "Smartphone confocal microscopy for imaging cellular structures in human skin in vivo," Biomed. Opt. Express **9**(4), 1906–1915 (2018).
9. J. M. Jabbour, S. Cheng, B. H. Malik, R. Cuenca, J. A. Jo, J. Wright, Y. S. Cheng, and K. C. Maitland, "Fluorescence lifetime imaging and reflectance confocal microscopy for multiscale imaging of oral precancer," J. Biomed. Opt. **18**(04), 1 (2013).
10. J. M. Jabbour, B. H. Malik, C. Olsovsky, R. Cuenca, S. Cheng, J. A. Jo, Y. S. Cheng, J. M. Wright, and K. C. Maitland, "Optical axial scanning in confocal microscopy using an electrically tunable lens," Biomed. Opt. Express **5**(2), 645–652 (2014).
11. Y. Nakai, M. Ozeki, T. Hiraiwa, R. Tanimoto, A. Funahashi, N. Hiroi, A. Taniguchi, S. Nonaka, V. Boilot, R. Shrestha, J. Clark, N. Tamura, V. M. Draviam, and H. Oku, "High-speed microscopy with an electrically tunable lens to image the dynamics of in vivo molecular complexes," Review of Scientific Instruments **86**(1), 013707 (2015).
12. W. J. Shain, N. A. Vickers, B. B. Goldberg, T. Bifano, and J. Mertz, "Extended depth-of-field microscopy with a high-speed deformable mirror," Opt. Lett. **42**(5), 995–998 (2017).
13. S. Quirin, D. S. Peterka, and R. Yuste, "Instantaneous three-dimensional sensing using spatial light modulator illumination with extended depth of field imaging," Opt. Express **21**(13), 16007–16021 (2013).
14. N. Koukourakis, M. Finkeldey, M. Sturmer, C. Leithold, N. C. Gerhardt, M. R. Hofmann, U. Wallrabe, J. W. Czarske, and A. Fischer, "Axial scanning in confocal microscopy employing adaptive lenses (CAL)," Opt. Express **22**(5), 6025–6039 (2014).
15. A. Badon, S. Bensussen, H. J. Gritton, M. R. Awal, C. V. Gabel, X. Han, and J. Mertz, "Video-rate large-scale imaging with Multi-Z confocal microscopy," Optica **6**(4), 389 (2019).
16. J. M. Tsang, H. J. Gritton, S. L. Das, T. D. Weber, C. S. Chen, X. Han, and J. Mertz, "Fast, multiplane line-scan confocal microscopy using axially distributed slits," Biomed. Opt. Express **12**(3), 1339–1350 (2021).
17. S. Xiao, H. Gritton, H.-A. Tseng, D. Zemel, X. Han, and J. Mertz, "High-contrast multifocus microscopy with a single camera and z-splitter prism," Optica **7**(11), 1477 (2020).
18. B. F. Grewe, F. F. Voigt, M. van 't Hoff, and F. Helmchen, "Fast two-layer two-photon imaging of neuronal cell populations using an electrically tunable lens," Biomed. Opt. Express **2**(7), 2035–2046 (2011).
19. A. D. Edelstein, M. A. Tsuchida, N. Amodaj, H. Pinkard, R. D. Vale, and N. Stuurman, "Advanced methods of microscope control using muManager software," J Biol Methods **1**(2), e10 (2014).
20. R. W. Cole, T. Jinadasa, and C. M. Brown, "Measuring and interpreting point spread functions to determine confocal microscope resolution and ensure quality control," Nat Protoc **6**(12), 1929–1941 (2011).
21. J. S. Benjamin Schmid, Albert Cardona, Mark Longair, and Martin Heisenberg, "A high-level 3D visualization API for Java and ImageJ," BMC Bioinformatics **11**, 274 (2010).
22. D. G. Roberts, H. B. Johnsonbaugh, R. D. Spence, and A. MacKenzie-Graham, "Optical Clearing of the Mouse Central Nervous System Using Passive CLARITY," J Vis Exp **11**(112), 54025 (2016).
23. L. Chen, M. Ghilardi, J. J. C. Busfield, and F. Carpi, "Electrically Tunable Lenses: A Review," Front. Robot. AI **8**, 678046 (2021).
24. K. Lee, E. Chung, S. Lee, and T. J. Eom, "High-speed dual-layer scanning photoacoustic microscopy using focus tunable lens modulation at resonant frequency," Opt. Express **25**(22), 26427–26436 (2017).
25. G. J. Goldey, D. K. Roumis, L. L. Glickfeld, A. M. Kerlin, R. C. Reid, V. Bonin, D. P. Schafer, and M. L. Andermann, "Removable cranial windows for long-term imaging in awake mice," Nat Protoc **9**(11), 2515–2538 (2014).
26. T. Yardeni, M. Eckhaus, H. D. Morris, M. Huizing, and S. Hoogstraten-Miller, "Retro-orbital injections in mice," Lab Anim **40**(5), 155–160 (2011).

27. T. L. Shiqing Li, Y. Luo, H. Yu, Y. Sun, H. Zhou, X. Liang, J. Huang, and S. Tang, "Retro-orbital injection of FITC-dextran is an effective and economical method for observing mouse retinal vessels," Molecular Vision **17**, 3566–3573 (2011).
28. M. Martinez-Corral, P.-Y. Hsieh, A. Doblas, E. Sanchez-Ortiga, G. Saavedra, and Y.-P. Huang, "Fast Axial-Scanning Widefield Microscopy With Constant Magnification and Resolution," J. Disp. Technol. **11**(11), 913–920 (2015).
29. S. Li, J. Wu, H. Li, D. Lin, B. Yu, and J. Qu, "Rapid 3D image scanning microscopy with multi-spot excitation and double-helix point spread function detection," Opt. Express **26**(18), 23585–23593 (2018).
30. T. Zhang, O. Hernandez, R. Chrapkiewicz, A. Shai, M. J. Wagner, Y. Zhang, C. H. Wu, J. Z. Li, M. Inoue, Y. Gong, B. Ahanonu, H. Zeng, H. Bito, and M. J. Schnitzer, "Kilohertz two-photon brain imaging in awake mice," Nat Methods **16**(11), 1119–1122 (2019).
31. R. Lu, M. Tanimoto, M. Koyama, and N. Ji, "50 Hz volumetric functional imaging with continuously adjustable depth of focus," Biomed. Opt. Express **9**(4), 1964–1976 (2018).
32. B. Chen, X. Huang, D. Gou, J. Zeng, G. Chen, M. Pang, Y. Hu, Z. Zhao, Y. Zhang, Z. Zhou, H. Wu, H. Cheng, Z. Zhang, C. Xu, Y. Li, L. Chen, and A. Wang, "Rapid volumetric imaging with Bessel-Beam three-photon microscopy," Biomed. Opt. Express **9**(4), 1992–2000 (2018).
33. S. Takanezawa, T. Saitou, and T. Imamura, "Wide field light-sheet microscopy with lens-axicon controlled two-photon Bessel beam illumination," Nat Commun **12**(1), 2979 (2021).
34. F. O. Fahrbach, V. Gurchenkov, K. Alessandri, P. Nassoy, and A. Rohrbach, "Light-sheet microscopy in thick media using scanned Bessel beams and two-photon fluorescence excitation," Opt. Express **21**(11), 13824–13839 (2013).
35. Y. Qu and Y. Hu, "Analysis of axial scanning range and magnification variation in wide-field microscope for measurement using an electrically tunable lens," Microsc Res Tech **82**(2), 101–113 (2019).
36. M. Saxena, G. Eluru, and S. S. Gorthi, "Structured illumination microscopy," Adv. Opt. Photonics **7**(2), 241 (2015).
37. M. M. Qureshi, Y. Liu, K. D. Mac, M. Kim, A. M. Safi, and E. Chung, "Quantitative blood flow estimation in vivo by optical speckle image velocimetry," Optica **8**(8), 1092 (2021).
38. T. E. Kornfield and E. A. Newman, "Measurement of Retinal Blood Flow Using Fluorescently Labeled Red Blood Cells," eNeuro **2**(2), ENEURO.0005-15.2015 (2015).
39. P. Y. Chhatbar and P. Kara, "Improved blood velocity measurements with a hybrid image filtering and iterative Radon transform algorithm," Front. Neurosci. **7**, 106 (2013).
40. J. Jiang, D. Zhang, S. Walker, C. Gu, Y. Ke, W. H. Yung, and S. C. Chen, "Fast 3-D temporal focusing microscopy using an electrically tunable lens," Opt. Express **23**(19), 24362–24368 (2015).
41. Z. Yang, Q. Tan, D. Cheng, L. Zhang, J. Zhang, E. W. Gu, W. Fang, X. Lu, and X. Liu, "The Changes of Intrinsic Excitability of Pyramidal Neurons in Anterior Cingulate Cortex in Neuropathic Pain," Front. Cell. Neurosci. **12**, 436 (2018).
42. J. Demas, J. Manley, F. Tejera, K. Barber, H. Kim, F. M. Traub, B. Chen, and A. Vaziri, "High-speed, cortex-wide volumetric recording of neuroactivity at cellular resolution using light beads microscopy," Nat Methods **18**(9), 1103–1111 (2021).
43. M. B. Bouchard, V. Voleti, C. S. Mendes, C. Lacefield, W. B. Grueber, R. S. Mann, R. M. Bruno, and E. M. Hillman, "Swept confocally-aligned planar excitation (SCAPE) microscopy for high speed volumetric imaging of behaving organisms," Nature Photon **9**(2), 113–119 (2015).
44. R. Tomer, M. Lovett-Barron, I. Kauvar, A. Andalman, V. M. Burns, S. Sankaran, L. Grosenick, M. Broxton, S. Yang, and K. Deisseroth, "SPED Light Sheet Microscopy: Fast Mapping of Biological System Structure and Function," Cell **163**(7), 1796–1806 (2015).
45. S. Ryu, B. Seong, C.-w. Lee, M. Y. Ahn, W. T. Kim, K.-M. Choe, and C. Joo, "Light sheet fluorescence microscopy using axi-symmetric binary phase filters," Biomed. Opt. Express **11**(7), 3936 (2020).
46. H. He, C. Kong, X. J. Tan, K. Y. Chan, Y. X. Ren, K. K. Tsia, and K. K. Y. Wong, "Depth-resolved volumetric two-photon microscopy based on dual Airy beam scanning," Opt. Lett. **44**(21), 5238–5241 (2019).
47. R. Liu, Z. Li, J. S. Marvin, and D. Kleinfeld, "Direct wavefront sensing enables functional imaging of infragranular axons and spines," Nat Methods **16**(7), 615–618 (2019).
48. Y.-K. Fuh, J.-K. Chen, and P.-W. Chen, "Characterization of electrically tunable liquid lens and adaptive optics for aberration correction," Optik **126**(24), 5456–5459 (2015).
49. T. Deguchi, P. Bianchini, G. Palazzolo, M. Oneto, A. Diaspro, and M. Duocastella, "Volumetric Lissajous confocal microscopy with tunable spatiotemporal resolution," Opt. Lett. **11**(11), 6293–6310 (2020).
50. J. Zheng, C. Zuo, P. Gao, and G. U. Nienhaus, "Dual-mode phase and fluorescence imaging with a confocal laser scanning microscope," Opt Lett **43**(22), 5689–5692 (2018).
51. E. M. Alexandre Mermillod-Blondin and C. B. Arnold, "High-speed varifocal imaging with a tunable acoustic gradient index of refraction lens," Opt. Lett. **33**(18), 2146–2148 (2008).
52. T. Chakraborty, B. Chen, S. Daetwyler, B. J. Chang, O. Vanderpoorten, E. Sapoznik, C. F. Kaminski, T. P. J. Knowles, K. M. Dean, and R. Fiolka, "Converting lateral scanning into axial focusing to speed up three-dimensional microscopy," Light Sci Appl **9**(1), 165 (2020).
53. J. Mertz, "Strategies for volumetric imaging with a fluorescence microscope," Optica **6**(10), 1261 (2019).
54. R. Shi, C. Jin, H. Xie, Y. Zhang, X. Li, Q. Dai, and L. Kong, "Multi-plane, wide-field fluorescent microscopy for biodynamic imaging in vivo," Biomed. Opt. Express **10**(12), 6625–6635 (2019).